Sodium-Ion Storage in Pyroprotein-Based Carbon Nanoplates

Young Soo Yun, Kyu-Young Park, Byoungju Lee, Se Youn Cho, Young-Uk Park, Sung Ju Hong, Byung Hoon Kim, Hyeokjo Gwon, Haegyeom Kim, Sungho Lee, Yung Woo Park, Hyoung-Joon Jin, and Kisuk Kang**

The development of low-cost and high-performance battery systems is essential for effective electricity utilization. Na-ion batteries (NIBs) are leading candidates for large-scale electricity storage as they are low cost and reserves of Na mineral salts are widespread.[1–3] Because battery performance is critically dependent on the electrode, the development of electrode materials is a crucial step in advancement of NIBs. In lithium-ion batteries (LIBs), graphite as an anode material plays a pivotal role in successful commercial application.[4,5] A layered host structure composed of sp^2 carbon bonds can store lithium ions reversibly up to LiC_6 (372 mA h g^{-1}) at a low potential of 0.1 V versus Li^+/Li.[5] The low-cost, readily available and well-appointed large-scale carbon-material processing systems are other advantages. However, the fundamental differences between lithium and sodium have limited the intercalation of sodium ions into graphite in an anodic potential, and while graphite possesses several important advantages as an anodic material, the inadequacy of graphite for NIBs has retarded the advancement of NIBs considerably.[6,7] Various alternative materials based on metal oxides, phosphides, and phosphorous have been investigated as possible anode materials for NIBs.[8–17] Although these materials have potential advantages for NIB anodes, there are limitations such as poor cyclic stability and high-cost and complex synthetic processes.

Carbon-based materials other than graphite have also been investigated as anode materials for NIBs due to their electrochemical activity with sodium.[18–27] Earlier works focused on disordered graphitic carbons (hard carbons), which showed reasonably high sodium capacity and low redox potential of around 0.1 V versus Na^+/Na.[28] However, they were generally found to have poor rate performance and cyclic stability. Nanostructured amorphous carbons (NACs) have also been demonstrated as high-power anode materials for NIBs.[20–24] Although despite their large ionic size sodium ions can be stored as rapidly as lithium ions in NACs, the average potential versus Na^+/Na was relatively high when used as an anode (>1 V).[20–24] More recently, nanostructured polymeric carbons (NPCs) prepared by high-temperature heat treatment (1000–1600 °C) showed a significantly lower sodium storage potential, below 0.1 V versus Na^+/Na, even with microstructures similar to NACs. Nonetheless, its power capability was lower than that of NACs.[18,19,25–27]

This series of carbon-based anodes and their distinct electrochemical properties in combination with sodium imply that crystalline structures of carbon may have a marked effect on sodium-ion storage behavior, which may be a critical factor in determining or tuning the electrochemical performance of these materials for NIBs. Despite the practical importance of carbonaceous materials for NIBs, the correlation between carbon local structure and sodium-ion storage is not clearly understood. In this study, we demonstrate that different carbon local orderings lead to substantially diverse electrochemical properties within morphologically identical carbon materials. To decouple the effects of local structure and morphology, nanoplates with different carbon orderings were fabricated using a silk protein platform, one of the most abundant biopolymers, via self-assembly and controlled pyrolysis. Through this process, six representative pyroprotein-based carbon nanoplates (CNPs) with varying degrees of carbon ordering were obtained; moreover, the shape of the nanoplates was maintained. We found that the sodium-ion storage mechanism varies from chemi-/physisorption, insertion to nanoclustering of metallic states, depending on the carbon structure of CNPs, which display various potentials and capacities. These results provide insights for further tuning of carbon-based materials for anodes of NIBs and improve understanding of sodium-ion storage behavior in carbonaceous materials.

Various CNP samples with different local carbon ordering were obtained by heating of a regenerated silk fibroin films and

Dr. Y. S. Yun, K.-Y. Park, B. Lee, Dr. Y.-U. Park, H. Gwon, Dr. H. Kim, Prof. K. Kang
Department of Materials Science and Engineering
Seoul National University
Seoul 151-742, South Korea
E-mail: matlgen1@snu.ac.kr
Dr. S. Y. Cho, Prof. H.-J. Jin
Department of Polymer Science and Engineering
Inha University
Incheon 402-751, South Korea
E-mail: hjjin@inha.ac.kr
S. J. Hong, Prof. Y. W. Park
Department of Physics and Astronomy
Seoul National University
Seoul 151-747, South Korea
Prof. B. H. Kim
Department of Physics
Incheon National University
Incheon 406-772, South Korea
Dr. S. Lee
Carbon Convergence Materials Research Center
Korea Institute of Science and Technology
Wanju-gun 565-905, South Korea
DOI: 10.1002/adma.201502303

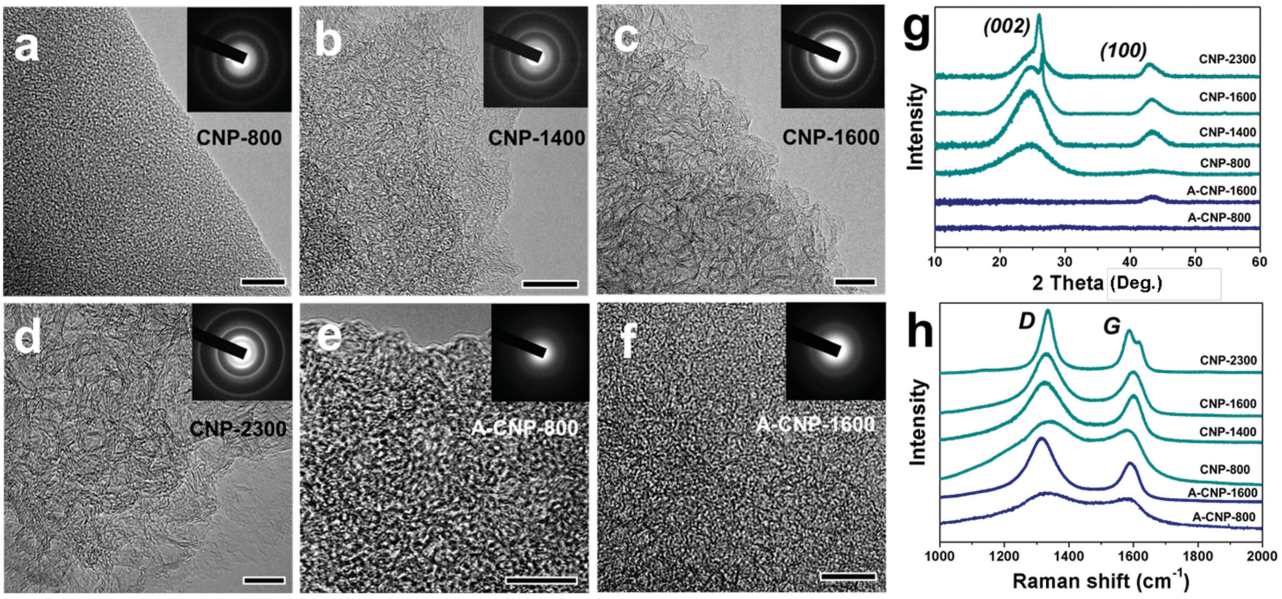

Figure 1. Pyroprotein-based carbon nanoplates (CNPs) and activated carbon nanoplates (A-CNPs) fabricated from regenerated silk protein. a–d) FE-TEM images of CNPs prepared at different heat-treated temperatures (HTTs) of 800, 1400, 1600, and 2300 °C. Graphitic structures gradually grew with increasing HTT. e) FE-TEM image of A-CNPs containing numerous sub-nanometer pores. The A-CNPs have a high surface area of 2557 m^2 g^{-1} and mainly ≈0.6 nm pores. f) FE-TEM image of the A-CNPs heat-treated at 1600 °C. Graphitic structures of A-CNPs barely grew at a HTT at 1600 °C. g) XRD data and h) Raman spectra of the samples.

following exfoliation (see Supporting Information including Figure S1 and S2 for details).[28–35] The exfoliated CNPs had nanoplate shapes with a height of 20–118 nm and a lateral size of ≈several micrometers (Figure S3 and S4, Supporting Information). The graphitic local structure developed gradually in the nanoplates with increasing temperatures from 800 to 2300 °C (**Figure 1**a,d). [35] Field-emission transmission electron microscopy (FE-TEM) images of CNP heat-treated at 800 °C (CNP-800) revealed an amorphous carbon structure (Figure 1a). Heat treatment to 1400, 1600, and 2300 °C (CNP-1400, CNP-1600, and CNP-2300) resulted in the gradual development of the local graphitic structure which was oriented randomly over the entire area (Figure 1b–d,g). Note that the (100) peaks appeared from CNP-1400 as shown in Figure 1g, indicating the development of an ordered hexagonal structure. Also, the abrupt change of G and D bands between CNP-800 and CNP-1400 in the Raman spectra (Figure 1h) supports the X-ray diffraction (XRD) results. These developments of graphitic structure caused the enhancement of electrical properties ranging from 10^0 to 10^2 S cm^{-1} at 300 K, as shown in Figure S5 (Supporting Information). However, despite more ordered structures, the densities of CNP-1400 and CNP-1600 were lower than that of CNP-800, indicating the presence of larger numbers of closed pores that are presumed to have developed during graphitization (Table S1, Supporting Information). The detailed characterization of CNP-1400, CNP-1600, and CNP-2300 can be found in Figure S3–S5 (Supporting Information).

Other types of CNP samples were prepared by heating of the silk fibroin/KOH mixture films at 800 °C (A-CNP-800) and following thermal annealing at 1600 °C (A-CNP-1600) (see Figure S6 in the Supporting Information). The FE-TEM image of A-CNP-800 shows nongraphitic local structure and pores developing within the nanoplates due to the KOH activation step (Figure 1e).[36] The nitrogen adsorption and desorption isotherm curves of A-CNP-800 confirmed an IUPAC type-I shape, indicative of a microporous structure (Fig. S6c, Supporting Information). Most of the pores were in the sub-nanometer range, primarily 0.6 nm in size (inset of Figure S6c, Supporting Information), resulting in a high specific surface area of 2557 m^2 g^{-1}, which is ≈120 times higher than that of CNP samples (≈20 m^2 g^{-1}). The XRD data for A-CNP-800 showed no noticeable peak (Figure 1g). In contrast, the Raman spectrum for A-CNP-800 indicated the presence of a hexagon plane with broad D and G bands (Figure 1h). These results suggest that the basic structural unit (BSU) of A-CNP-800 is composed of highly defective and poorly stacked hexagonal planes. In the case of A-CNP-1600, a more ordered carbon structure was observed (Figure 1f). However, compared to CNP-1600, the graphitic structure was far less developed, as shown in Figure 1g,h. The detailed characterization of A-CNP-800 and A-CNP-1600 can be also found in Figure S6 (Supporting Information).

The electrochemical properties of CNPs with different degrees of crystalline ordering were investigated using a half-cell test with sodium metal foil as both the reference and counter electrodes in an electrolyte containing 1 M $NaPF_6$ dissolved in diethylene glycol dimethyl ether (DEGDME). The galvanostatic discharge/charge curves shown in **Figure 2**a vary considerably between samples, indicating dissimilar sodium-ion storage behaviors. The discharge (sodium insertion) profiles of electrodes exhibited three distinct sections: i) a linear voltage drop occurring mainly in the range 2.5–0.7 V, ii) a gradual voltage decay around 0.7–0.1 V, and (3) a plateau at 0.1 V. These three distinct sections are evident in Figure 2b, in which three representative samples of A-CNP-800, CNP-800,

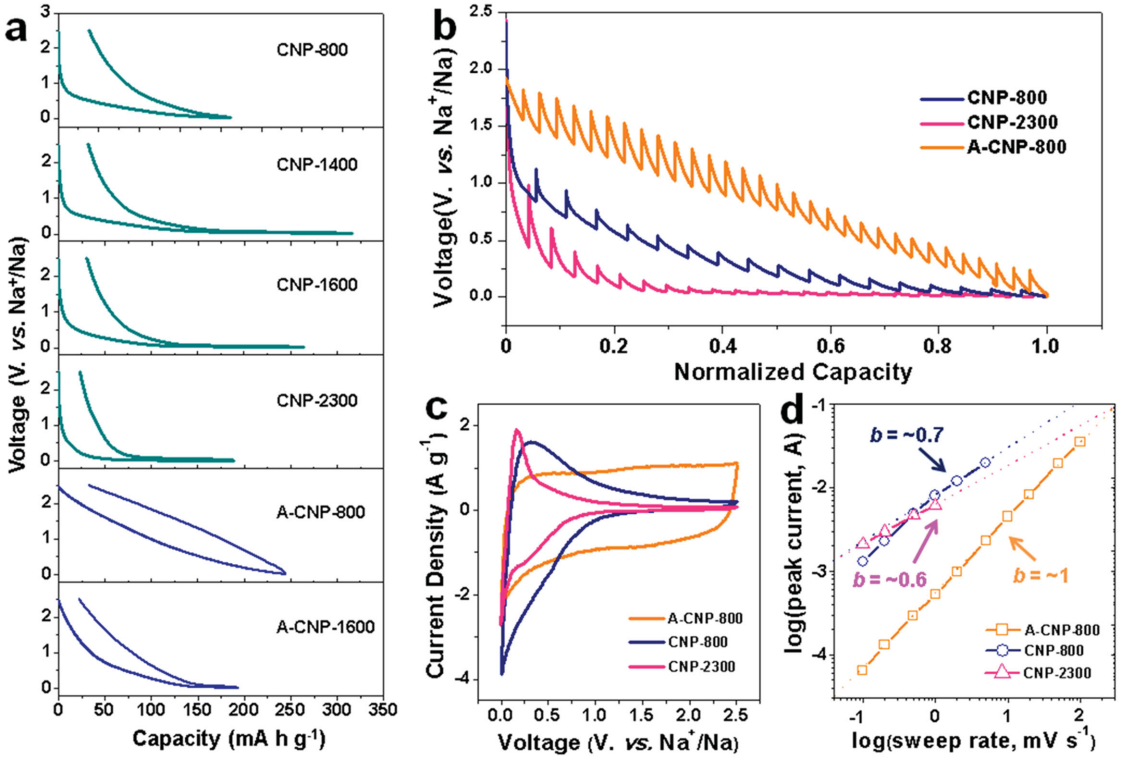

Figure 2. Electrochemical properties of CNPs and A-CNPs. a) Galvanostatic 2nd discharge/charge profiles of all samples at a current density of 50 mA g^{-1} in a potential range of 0.005 to 2.5 V versus Na^+/Na in an electrolyte of 1 M $NaPF_6$ dissolved in diethylene glycol dimethyl ether (DEGDME). b) Quasi-open-circuit potential data measured at a current density of 20 mA g^{-1} with a rest time of 6 h. c) Cyclic voltammograms of CNP-800, CNP-2300, and A-CNP-800 at a sweep rate of 5 mV s^{-1}. The representative samples depict their distinctive sodium-ion storage behaviors. d) Voltammetric current dependence on the sweep rate. The *b*-values of A-CNP-800, CNP-800, and CNP-2300 were 1, 0.7, and 0.6, respectively.

and CNP-2300 are shown. Quasi-open-circuit potential (QOCP) measurements demonstrated that the discharge profiles can be deconvoluted into a linear segment between 2.5 and 0.7 V (A-CNP-800), a curved section between 0.7 and 0.1 V (CNP-800), and a plateau at 0.1 V (CNP-2300) (Figure 2b). The designation of each section to a specific sodium-ion storage mechanism is undertaken using cyclovoltammograms (CV) and the time-dependent electrochemical response of the electrodes. Figure 2c shows that the CV curve of A-CNP-800 follows a near rectangular shape, which is characteristic of capacitive charge storage by surface adsorption/desorption of ions. These capacitive charge-storage mechanisms can be confirmed by varying the sweep rate of the CV in the range 0.1–100 mV s^{-1}, as shown in Figure 2d. Assuming that the current obeys a power-law relationship as a function of voltage, $i = av^b$, during the sweep, where a and b are constants, the data can be fitted using $b \approx 1$, suggesting that the electrochemical reaction is mostly surface-controlled.[37,38] It is noteworthy that the surface area of A-CNP-800 was 2557 m^2 g^{-1}—about 120-fold higher than the other samples. Large charge storage is, therefore, possible as a form of electrostatic charge accumulation (physisorption) at the electrode/electrolyte interfaces. Since A-CNP-800 is composed of highly defective hexagonal planes, faradic reactions (chemisorption) at the defective planes may also be expected. A density functional theory (DFT) calculation found that defect sites in the basal plane of graphene could behave as a redox center for sodium-ion chemisorption, with a calculated potential of 0.05–0.87 V. As shown in **Figure 3**, various structural defects can contribute to sodium-ion storage at sites such as carbon vacancies (type 1), carbon divacancies (types 2, 3, and 4), carbon site changes (type 5), and adatoms (type 6).[39] It was observed that larger defect sites exhibit a higher potential for sodium-ion chemisorption, e.g., heptagonal sites (red in Figure 3b) show higher sodium-ion chemisorption potentials than those of pentagonal sites (blue), mostly likely due to the large size of the sodium ion.[40] In contrast, in a perfect graphene structure (no defects) and nitrogen-substituted graphene (type 7) sodium-ion chemisorption was found to be inactive, as shown in Figure 3b. These results demonstrate the feasibility of sodium-ion chemisorption, particularly in A-CNP-800 with a large number of defect sites. Edge sites of graphite or graphene were not considered because these sites are likely to be terminated with heteroatoms such as hydrogen and functional groups, in which redox reactions are more complex and accurate modeling is more difficult.[41]

In contrast, the CV of CNP-800 (Figure 2c) showed a continuous increase in the cathodic current (sodium insertion) mainly at voltages below 1 V. This is consistent with the curved profile of CNP-800 in the QOCP result shown in Figure 2b. The gradual decrease in voltage is likely due to the range of local environments available for sodium ions in CNP-800, which contains pseudographitic carbons. In this voltage range, the chemisorption of sodium ion is also expected to occur to some extent due to the defective nature of CNP-800 crystallites, and

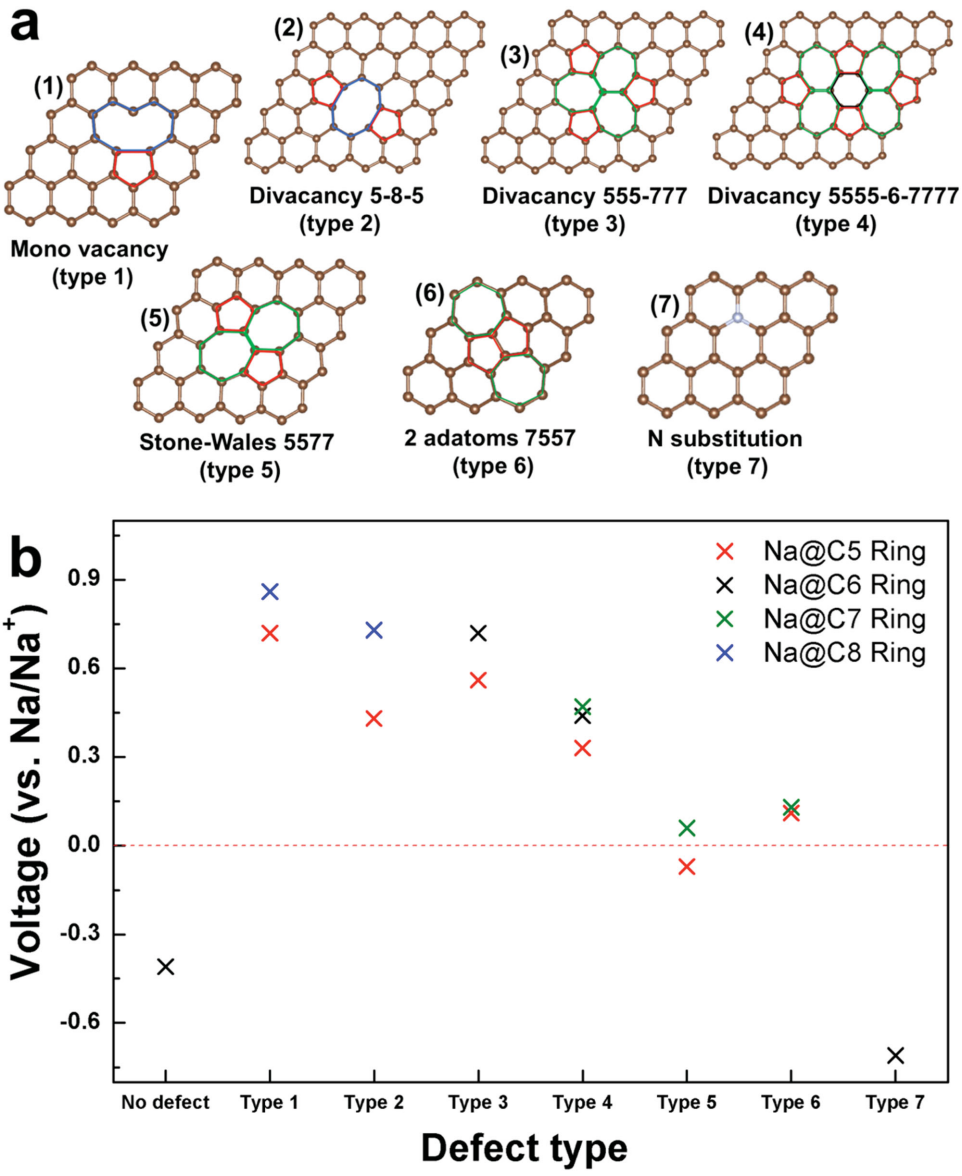

Figure 3. Sodium-ion storage in various defect sites on a basal plane of graphene based on first-principles calculation. a) Schematic images of defect sites in basal plane of graphene: (1) carbon vacancy (type 1), (2–4) carbon divacancy (types 2, 3, and 4), (5) carbon site change (type 5), (6) adatoms (type 6), and (7) nitrogen-substituted graphene (type 7). b) Density functional theory calculation data for chemisorption energy of given defect site with sodium ion. Their potentials were calculated to be 0.05–0.87 V, indicating that sodium ions can be stored in the defect sites.

the observed voltage well corresponds to the calculated chemisorption voltage range. However, physisorption in CNP-800 is likely to be insignificant because of the low surface area (by two orders of magnitude) compared to A-CNP-800. Notably, a similar voltage profile below 1 V was recently reported by Wen et al. Sodium ions can be inserted in expanded graphite interlayers (≈4.3 Å), suggesting that a sodium insertion reaction may be possible in the pseudographitic carbon structure of CNP-800.[18,26,42,43] The direct evidence of sodium insertion was not trivial to obtain due to the broad nature of the XRD peaks of pristine CNP-800. However, ex situ XRD data for CNP-800 reveal that the graphitic (002) peak in the pristine electrode changed significantly through the various stages of electrochemical cycling. **Figure 4**a clearly shows that the (002) peak broadened markedly after discharge to 0.005 V and recovered after charge to 2.5 V at a slightly smaller angle. This change in the peak intensity was also reversibly observed throughout cycling, confirming a reversible change in graphitic layer orderings with sodium insertion and extraction. It is likely that the nonuniform insertion of sodium ions significantly disorders the interlayer distance and stacking sequence of graphene layers in the graphitic region, thus causing broadening of the (002) peak. Moreover, the extraction of sodium partially recovers the layered structure, while leaving stacking faults behind, shifting the center of the (002) peak to the smaller angle of 20.1°. While the results suggest that sodium ions were inserted into the pseudo-

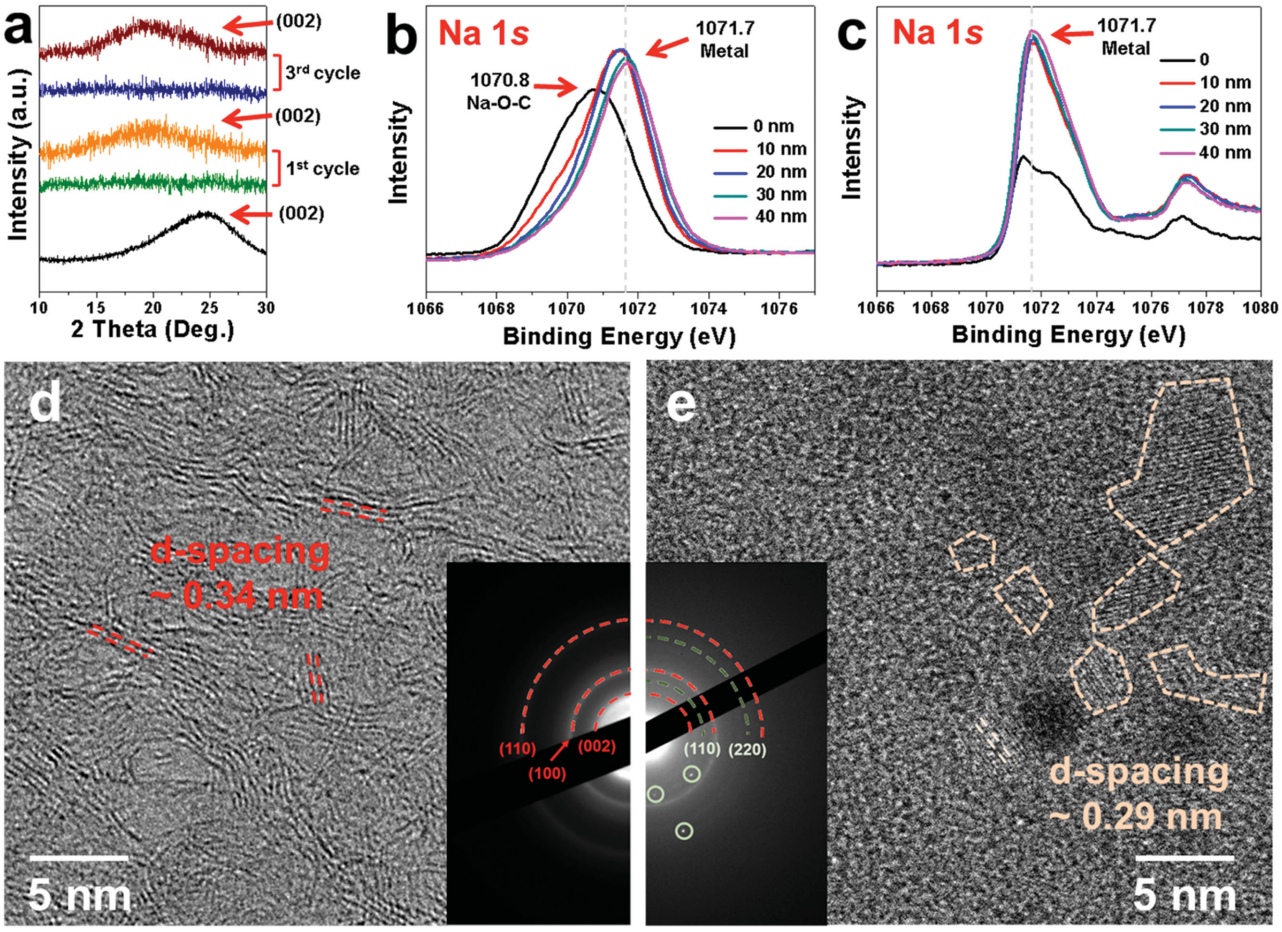

Figure 4. Ex situ characterization of CNP-800 and CNP-2300. a) XRD data of pristine CNP-800 electrode (black) and ex situ CNP-800 electrodes after first discharge (olive) and charge (orange), and third discharge (navy) and charge (wine). b) Ex situ XPS Na 1s spectra depth profiles of CNP-2300 after discharging (Na insertion) to 0.005 V and c) XPS Na 1s spectra depth profiles of Na metal foil. d) HR-TEM image of the CNP-2300 sample. The CNP-2300 has a graphitic structure with (002), (100), and (110) crystal faces, and e) ex situ HR-TEM image of the CNP-2300 sample after discharging (Na insertion) to 0.005 V. Na metal nanoclusters were found in the CNP-2300 sample after Na insertion. This suggests that sodium ions are reduced in the disordered graphitic structures to sodium metal nanoclusters.

graphitic layers, this differs from conventional intercalation in which the insertion sites of sodium ions are not hexagonal carbon sites since they are not energetically favorable, but likely to be mainly defective domains.[44] The voltage sweep experiment in Figure 2d exhibited a *b* value less than unity (≈0.7) indicating the interplay between surface-controlled and diffusion-controlled reactions. This result also supports the hypothesis that sodium ions are stored by chemi-/physisorption at defect sites along with diffusion-limited sodium insertion reactions.

In the case of CNP-2300, the CV shows a relatively sharp peak around 0.1 V in Figure 2c. The peak at 0.1 V also corresponds to the voltage plateau of the CNP samples in Figure 2a,b. After a full discharge, a postmortem analysis of the sample was performed to identify the primary reaction in this region and showed the presence of Na-based compounds as shown in the X-ray photoelectron spectroscopy (XPS) in Figure 4b. In the XPS depth profiling of CNP-2300 in the Na 1s spectrum region, a peak of Na—O—C bonding centered at 1070.8 eV was found mainly along the outer surface of CNP-2300, which remained after Na extraction to 0.5 V, as shown in Figure S7 (Supporting Information). The Na—O—C bonding is believed to be from the solid electrolyte interphase layer formed on the electrode surface. In contrast, a peak centered at 1071.7 eV was observed mainly inside the sample after sodium insertion. Characterization using an Na metal foil revealed that the peak at 1071.7 eV is most likely from metallic sodium. As a reference, depth profiles of the Na metal foil from 10 to 40 nm were obtained in the same set of experiments. Figure 4c shows that the binding energy of metallic Na is observed at 1071.7 eV, after removing the surface oxide, suggesting that the metallic form of sodium is stored in CNP-2300. Moreover, the presence of Na metal in the CNP-2300 sample was directly confirmed by high-resolution TEM (HR-TEM) observations. The disordered structures of the nanosized graphitic domains with a *d*-spacing of ≈0.34 nm were observed in the as-prepared CNP-2300 sample, as shown in Figure 4d. After discharge (Na insertion) to 0.005 V, several Na metal nanoclusters were found in the same CNP-2300 sample (Figure 4e). The lattice spacing of 0.29 nm corresponds well to the (220) plane of BCC Na metal. The selected area electron

diffraction in the inset of Figure 4d,e clearly shows that (110) and (220) faces of Na metal appear after sodiation, indicating that the sodium ions were reduced to nanometer-scale metal clusters on the disordered graphitic structures. To the best of our knowledge, this is the first direct observation of metallic sodium storage in carbon-based electrodes. It should be noted that sodium metal nanoclustering in carbon at 0.1 V is distinct from plating of sodium metal on the surface of an electrode at 0 V. Nanopores present in the CNP-2300 are expected to provide more energetically stable sodium environments with a positive 0.1 V potential versus Na/Na^+.[45] The voltammetric current response of CNP-2300 in the varying sweep rates was fitted using $b = 0.6$, indicating a mainly diffusion controlled reaction (Figure 2d).[37,38]

These three characteristic sodium-ion storage behaviors were also observed in CNP-1400, CNP-1600, and A-CNP-1600. Interestingly, samples with more defective carbon structures showed greater capacities at 0.7–0.1 V. In addition, the capacities at the 0.1 V plateau are found to be dependent on the density of the samples. When the densities of the samples increase, the capacities in the plateaus decrease proportionally (Table S1, Supporting Information), suggesting that nanopores play an important role in reversible sodium-ion storage in the form of metallic nanoclustering.

The different local carbon ordering of CNPs enables versatile applications using a sodium-ion charge carrier. A-CNP-800 based on the fast chemi-/physisorption showed the highest power capability and cyclic stability, but had an unfavorable potential for use as an anode material for NIBs (see Figure S8a and S8b in the Supporting Information). These electrochemical characteristics of A-CNP-800 are more suitable as an anode material for asymmetric pseudocapacitor rather than NIBs. In contrast, CNP-1400 containing chemisorption, insertion, and nanoclustering showed the highest reversible capacity and the largest plateau at 0.1 V, indicating the highest energy density (see Figure S8c and S8d in the Supporting Information). Thus, with different counterparts such as commercially available porous carbon (AC) (MSP-20; Figure S9a, Supporting Information) and $Na_{1.5}VPO_{4.8}F_{0.7}$[46] (Figure S9b, Supporting Information) as a cathode, A-CNP-800 and CNP-1400 were used as anode materials for asymmetric sodium-ion pseudocapacitors (A-NIPs) and NIBs, respectively (Figure S10, Supporting Information). NIBs achieved a specific power and energy of 1603 W kg^{-1} and 117 W h kg^{-1}, respectively. The gravimetric power was higher in the A-NIPs, which showed a specific power of 4072 W kg^{-1} at a specific energy of 57 W h kg^{-1}. With further boosting, a specific power of 7763 W kg^{-1} was achieved for a 4s charge/discharge rate. These energy and power characteristics are considerably higher than those reported previously.[6,47–49]

In summary, 2D pyroprotein-based carbon nanostructures were successfully fabricated from a self-assembled silk protein nanoplate and used as a carbon platform to investigate sodium-ion storage behaviors in various local carbon orderings. Samples with different carbon structures exhibited different sodium-ion storage behaviors, which included physisorption, chemisorption, insertion or nanoclustering depending on the presence of defects and nanopores, and the surface area. A-CNP-800 with a highly porous and defective carbon structure displayed a primarily physi/chemisorption-based sodium-ion storage mechanism in the voltage range 2.5–0.7 V versus Na^+/Na. In contrast, CNP-800 with a large number of pseudographitic crystallites showed mixed chemisorption- and insertion-based sodium storage below 0.7 V, allowing sodium-ion insertion between the graphene layers. CNP-2300 with an ordered graphitic (100) structure and corresponding nanopores showed a plateau at 0.1 V, originating from nanoclustering of sodium metal, as confirmed by HR-TEM. The variety of electrochemical properties displaying distinct potentials and capacities and the straightforward dependency of these on the carbon structure imply that tailoring carbon orderings is a critical factor for tuning the electrochemical performance of carbonaceous materials for NIBs. The results of this study not only provide a better understanding of sodium-ion storage behavior in carbonaceous materials but also offer a design strategy for electrode optimization for various sodium-based electrochemical devices.

Experimental Section

Preparation of CNPs and A-CNPs: Bombyx mori silk fibroin solutions were prepared using a procedure reported elsewhere..[28,34,50] Cocoons of *B. mori* silkworm silk were boiled for 30 min in an aqueous solution of Na_2CO_3 (OCI company, 99%, 0.02 M) and rinsed thoroughly with water to remove the glue-like sericin proteins.[34] The extracted silk fibroin was then dissolved in an aqueous 9.3 M LiBr (Sigma–Aldrich, ≥99%) solution at room temperature to yield a 20 wt% solution. This solution was dialyzed in water using Slide-a-Lyzer dialysis cassettes (Pierce, MWCO 3500) for 48 h. The final concentration of the aqueous silk fibroin solution was 7.0–8.0 wt%. The solution was cast on a Petri dish to obtain a silk fibroin film with a thickness of ≈100 μm. The silk fibroin film was heated from room temperature to 800, 1400, 1600, and 2300 °C, respectively. A heating rate of 10 °C min^{-1} and an Ar flow of 200 mL min^{-1} were applied, including a middle and final step, whereby the samples were held at 350 °C and at the final temperature for 2 h, respectively. The carbonaceous material products were exfoliated in *N*-methyl-pyrrolidone (Sigma–Aldrich, 99.5%) using an ultrasound treatment. After vacuum filtration and washing with ethanol (Sigma–Aldrich, ≥99.5%), the final CNP products were stored in a vacuum oven at 30 °C.

KOH (12 g) was added to 100 g of aqueous silk fibroin solution. The silk fibroin/KOH mixture was stirred for 30 min and then cast in Teflon dishes. The cast solutions were dried in a convection oven at 120 °C for 3 d. The silk fibroin/KOH mixture films were heated from room temperature to 800 °C for 2 h at a heating rate of 10 °C min^{-1} and an Ar flow of 200 mL min^{-1}. The resulting carbonaceous materials were washed with distilled water and ethanol (Sigma–Aldrich, ≥99.5%), and dried in a vacuum oven at 30 °C. The product (A-CNP-800) was thermally treated at 1600 °C for 2 h at a heating rate of 10 °C min^{-1} and an Ar flow of 200 mL min^{-1}. The resulting material (A-CNP-1600) was stored in a vacuum oven at 30 °C.

Material Characterization: The morphologies of the CNPs were observed using FE-TEM (JEM2100F, JEOL, Japan) and FE-SEM (S-4300, Hitachi, Japan), and the topographies of CNPs were characterized using AFM (NT-MDT, Russia). Raman spectra were recorded using a continuous-wave linearly polarized laser with a wavelength of 514.5 nm (2.41 eV) and a power of 16 mW. The laser beam was focused using a 100× objective lens, resulting in a spot size with a diameter of around 1 μm. The acquisition time and number of circulations for collecting each spectrum were 10 s and five, respectively. XRD (Rigaku DMAX 2500) was carried out using Cu Kα radiation (wavelength $\lambda = 0.154$ nm) operated at 40 kV and 100 mA. The chemical composition of the samples was evaluated using XPS (PHI 5700 ESCA,

Chanhassen, MN, USA) with monochromatic Al Kα radiation ($h\nu$ = 1486.6 eV) and EA with an EA1112 (CE instrument, Italy). The FTIR was performed using VERTEX 80v (Bruker Optics, Germany). TGA data were obtained using a NETZSCH STA 409 PC Luxx simultaneous thermal analyzer (Germany) from room temperature to 800 °C at a heating rate of 10 °C min^{-1} under a nitrogen gas atmosphere. Densities of the CNPs were characterized using a pycnometer (Accupyc 1330, Gas pycnometer, USA). The porous properties of the CNPs were analyzed using nitrogen adsorption and desorption isotherms obtained using the surface area and a porosimetry analyzer (ASAP 2020, Micromeritics, USA) at −196 °C. To measure the electrical transport properties, CNPs were deposited on 300 nm thick SiO_2/highly p-doped Si wafers. The electrode was fabricated by conventional electron beam lithography (acceleration voltage: 15 kV). Ti/Au (5/50 nm) were deposited using an e-gun/therm evaporation system under high vacuum ($<1 \times 10^{-3}$ Pa) and lift-off procedures. Temperature-dependent *I–V* characteristics were determined by the conventional two-probe method in a Janis cryogenic system with a semiconductor characterization system (4200-SCS, Keithley). The electrical measurements were performed under vacuum (<0.2 Pa).

Ex Situ TEM Characterization: The ex situ TEM sample was prepared using a CR2032 coin-type cell. The copper-mesh TEM grid and working electrode including active materials were assembled in an argon-filled glove box with electrolyte. Na metal was used as a counter electrode and a glass microfiber filter (GF/F, Whatmant) as a separator. The coin cell was discharged to 0.005 V (vs Na/Na^+) and maintained at 0.005 V (vs Na/Na^+) until reaching thermodynamic equilibrium. After discharging, the coin cell was disassembled in an argon-filled glove box and the TEM grid was removed from the cell. The TEM grid was shrouded in dimethyl carbonate (DMC) electrolyte to limit exposure to air and then moved to the TEM machine. In this process, the TEM grid was exposed to air within 3–4 s.

Density Functional Calculation: First-principles calculations were conducted to determine energies of given structures based on a spin-polarized generalized gradient approximation (GGA) using a Perdew–Burke–Ernzerhof (PBE) exchange-correlation parameterization of DFT.[51] The projector-augmented wave (PAW) method was implemented in the Vienna ab initio simulation package (VASP).[52] All calculations were conducted for $6a \times 6b$ supercells for graphene sheet, along with 20 Å of vacuum slab to prevent self-interaction between sheets. A plane-wave basis set with a kinetic energy cutoff of 500 eV and reciprocal space k-point meshes of $2 \times 2 \times 1$ were used. All structures were fully relaxed.

Electrochemical Characterization: Sodium-ion storage behaviors were characterized using a Wonatec automatic battery cycler and CR2032-type coin cells. For the half-cell tests, the coin cells were assembled with the CNPs/A-CNPs as the working electrode, and metallic sodium foil as both the reference and counter electrodes in a glove box filled with argon. $NaPF_6$ (1 M; Aldrich, purity: 99.99%) was dissolved in a solution of DEGDME and used as the electrolyte. The working electrodes were prepared by mixing the active material (80 wt%) with conductive carbon (10 wt%) and poly(vinylidene fluoride) (10 wt%) in *N*-methyl-2-pyrrolidone. The resulting slurries were uniformly applied to the Al foil. The electrodes were dried at 120 °C for 2 h and roll pressed. The A-NIPs based on A-CNP-800/AC were assembled using precycled A-CNP-800 as the anode and ACs (MSP-20) as the cathode. The voltage was controlled to 2 V versus Na^+/Na. The NIBs based on CNP-1400/$Na_{1.5}VPO_{4.8}F_{0.7}$ were assembled using precycled CNP-1400 as the anode and $Na_{1.5}VPO_{4.8}F_{0.7}$ as the cathode. The pseudocapacitors and batteries were galvanostatically cycled between 0.5 and 4.0 V and 2.0 and4.3 V, respectively, at various currents.

Supporting Information

Supporting Information is available from the Wiley Online Library or from the author.

Acknowledgements

This work was supported by the Human Resources Development program (20124010203320) of the Korea Institute of Energy Technology Evaluation and Planning (KETEP) grant funded by the Korea government Ministry of Trade, Industry and Energy, and the Korea Institute of Science and Technology (KIST) Program. This work was also supported by Industrial Strategic Technoloy Development Program (Project No. 10050477) funded by the Ministry of Trade, Industry & Energy.

Received: May 13, 2015
Revised: July 11, 2015
Published online: September 30, 2015

[1] M. D. Slater, D. Kim, E. Lee, C. S. Johnson, *Adv. Funct. Mater.* **2013**, *23*, 947.
[2] S.-W. Kim, D.-H. Seo, X. Ma, G. Ceder, K. Kang, *Adv. Energy Mater.* **2012**, *2*, 710.
[3] V. Palomares, P. Serras, I. Villaluenga, K. B. Hueso, J. Carretero-González, T. Rojo, *Energy Environ. Sci.* **2012**, *5*, 5884.
[4] J.-M. Tarascon, M. Armand, *Nature* **2001**, *414*, 359.
[5] V. Etacheri, R. Marom, R. Elazari, G. Salitra, D. Aurbach, *Energy Environ. Sci.* **2011**, *4*, 3243.
[6] H. Kim, J. Hong, Y.-U. Park, J. Kim, I. Hwang, K. Kang, *Adv. Funct. Mater.* **2015**, *25*, 534.
[7] D. A. Stevens, J. R. Dahn, *J. Electrochem. Soc.* **2001**, *148*, A803.
[8] Y. Sun, L. Zhao, H. Pan, X. Lu, L. Gu, Y.-S. Hu, H. Li, M. Armand, Y. Ikuhara, L. Chen, X. Huang, *Nat. Commun.* **2013**, *4*, 1870.
[9] B. Koo, S. Chattopadhyay, T. Shibata, V. B. Prakapenka, C. S. Johnson, T. Rajh, E. V. Shevchenko, *Chem. Mater.* **2013**, *25*, 245.
[10] Y. Kim, Y. Kim, A. Choi, S. Woo, D. Mok, N.-S. Choi, Y. S. Jung, J. H. Ryu, S. M. Oh, K. T. Lee, *Adv. Mater.* **2014**, *26*, 4139.
[11] D. Y. W. Yu, P. V. Prikhodchenko, C. W. Mason, S. K. Batabyal, J. Gun, S. Sladkevich, A. G. Medvedev, O. Lev, *Nat. Commun.* **2013**, *4*, 2922.
[12] K. He, Y. Zhou, P. Gao, L. Wang, N. Pereira, G. G. Amatucci, K.-W. Nam, X.-Q. Yang, Y. Zhu, F. Wang, D. Su, *ACS Nano* **2014**, *8*, 7251.
[13] Y. Kim, Y. Park, A. Choi, N.-S. Choi, J. Kim, J. Lee, J. H. Rye, S. M. Oh, K. T. Lee, *Adv. Mater.* **2013**, *25*, 3045.
[14] J. Qian, X. Wu, Y. Cao, X. Ai, H. Yang, *Angew. Chem. Int. Ed.* **2013**, *52*, 4633.
[15] D. Su, H.-J. Ahn, G. Wang, *Chem. Commun.* **2013**, *49*, 3131.
[16] Y. Zhu, X. Han, Y. Xu, Y. Liu, S. Zheng, K. Xu, L. Hu, C. Wang, *ACS Nano* **2013**, *7*, 6378.
[17] W. Li, S.-L. Chou, J.-Z. Wang, J. H. Kim, H.-K. Liu, S.-X. Dou, *Adv. Mater.* **2014**, *26*, 4037.
[18] E. M. Lotfabad, J. Ding, K. Cui, A. Kohandehghan, W. P. Kalisvaart, M. Hazelton, D. Mitlin, *ACS Nano* **2014**, *8*, 7115.
[19] A. Ponrouch, A. R. Goñi, M. R. Palacín, *Electrochem. Commun.* **2013**, *27*, 85.
[20] Z. Wang, L. Qie, L. Yuan, W. Zhang, X. Hu, Y. Huang, *Carbon* **2013**, *55*, 328.
[21] H.-G. Wang, Z. Wu, F.-L. Meng, D.-L. Ma, X.-L. Huang, L.-M. Wang, X.-B. Zhang, *ChemSusChem* **2013**, *6*, 56.
[22] L. Fu, K. Tang, K. Song, P. A. V. Aken, Y. Yu, J. Maier, *Nanoscale* **2014**, *6*, 1384.
[23] K. Tang, L. Fu, R. J. White, L. Yu, M.-M. Titirici, M. Antonietti, J. Maier, *Adv. Energy Mater.* **2012**, *2*, 873.
[24] Y.-X. Wang, S.-L. Chou, H.-K. Liu, S.-X. Dou, *Carbon* **2013**, *57*, 202.
[25] W. Luo, J. Schardt, C. Bommier, B. Wang, J. Razink, J. Simonsen, X. Ji, *J. Mater. Chem. A* **2013**, *1*, 10662.

[26] J. Ding, H. Wang, Z. Li, A. Kohandehghan, K. Cui, Z. Xu, B. Zahiri, X. Tan, E. M. Lotfabad, B. C. Olsen, D. Mitlin, *ACS Nano* **2013**, *7*, 11004.
[27] Y. Li, S. Xu, X. Wu, J. Yu, Y. Wang, Y.-S. Hu, H. Li, L. Chen, X. Huang, *J. Mater. Chem A* **2015**, *3*, 71.
[28] D. A. Stevens, J. R. Dahn, *J. Electrochem. Soc.* **2000**, *147*, 1271.
[29] H.-S. Kim, S.-H. Yoon, S.-M. Kwon, H.-J. Jin, *Biomacromolecules* **2009**, *10*, 82.
[30] H.-J. Jin, D. L. Kaplan, *Nature* **2003**, *424*, 1057.
[31] Y. Takahashi, M. Gehoh, K. Yuzuriha, *Int. J. Biol. Macromol.* **1999**, *24*, 127.
[32] S.-W. Ha, H. S. Gracz, A. E. Tonelli, S. M. Hudson, *Biomacromolecules* **2005**, *6*, 2563.
[33] K. Numata, P. Cebe, D. L. Kaplan, *Biomaterials* **2010**, *31*, 2926.
[34] H.-J. Jin, J. Park, V. Karageorgiou, U.-J. Kim, R. Valluzzi, P. Cebe, D. L. Kaplan, *Adv. Funct. Mater.* **2005**, *15*, 1241.
[35] S. Y. Cho, Y. S. Yun, S. Lee, D. Jang, K.-Y. Park, J. K. Kim, B. H. Kim, K. Kang, D. L. Kaplan, H.-J. Jin, *Nat. Commun.* **2015**, *6*, 7145.
[36] J. Romanos, M. Beckner, T. Rash, L. Firlej, B. Kuchta, P. Yu, G. Suppes, C. Wexler, P. Pfeifer, *Nanotechnology* **2012**, *23*, 015401.
[37] V. Augustyn, J. Come, M. A. Lowe, J. W. Kim, P.-L. Taberna, S. H. Tolbert, H. D. Abruña, P. Simon, B. Dunn, *Nat. Mater.* **2013**, *12*, 518.
[38] V. Augustyn, P. Simon, B. Dunn, *Energy Environ. Sci.* **2014**, *7*, 1597.
[39] F. Banhart, J. Kotakoski, A. V. Krasheninnikov, *ACS Nano* **2011**, *5*, 26.
[40] R. D. Shannon, *Acta Cryst.* **1976**, *A32*, 751.
[41] H. Kim, Y.-U. Park, K.-Y. Park, H.-D. Lim, J. Hong, K. Kang, *Nano Energy* **2014**, *4*, 97.
[42] Y. Wen, K. He, Y. Zhu, F. Han, Y. Xu, I. Matsuda, Y. Ishii, J. Cumings, C. Wang, *Nat. Commun.* **2014**, *5*, 4033.
[43] S. Komaba, W. Murata, T. Ishikawa, N. Yabuuchi, T. Ozeki, T. Nakayama, A. Ogata, K. Gotoh, K. Fujiwara, *Adv. Funct. Mater.* **2011**, *21*, 3859.
[44] P.-C. Tsai, S.-C. Chung, S.-K. Lin, A. Yamada, *J. Mater. Chem. A* **2015**, *3*, 9763.
[45] D. A. Stevens, J. R. Dahn, *J. Electrochem. Soc.* **2001**, *148*, A803.
[46] Y.-U. Park, D.-H. Seo, H.-S. Kwon, B. Kim, J. Kim, H. Kim, I. Kim, H.-I. Yoo, K. Kang, *J. Am. Chem. Soc.* **2013**, *135*, 13870.
[47] L. Zhao, L. Qi, H. Wang, *J. Power Sources* **2013**, *242*, 597.
[48] Z. Chen, V. Augustyn, X. Jia, Q. Xiao, B. Dunn, Y. Lu, *ACS Nano* **2012**, *6*, 4319.
[49] J. Yin, L. Qi, H. Wang, *ACS Appl. Mater. Interfaces* **2012**, *4*, 2762.
[50] Y. S. Yun, S. Y. Cho, J. Shim, B. H. Kim, S.-J. Chang, S. J. Baek, Y. S. Huh, Y. Tak, Y. W. Park, S. Park, H.-J. Jin, *Adv. Mater.* **2013**, *25*, 1993.
[51] J. P. Perdew, K. Burke, M. Ernzerhof, *Phys. Rev. Lett.* **1996**, *77*, 3865.
[52] G. Kresse, J. Furthmüller, *Comput. Mater Sci.* **1996**, *6*, 15.